ORIGINAL PAPER

physica status solidi b

www.pss-b.com

Electronic and Magnetic Properties of $BaFeO_3$ on the Pt(111) Surface in a Quasicrystalline Approximant Structure

Waheed Adeniyi Adeagbo, Igor V. Maznichenko, Hichem Ben Hamed, Ingrid Mertig, Arthur Ernst, and Wolfram Hergert*

Perovskite-like ABO_3 oxides A = (Ca, Sr, Ba) and B = (Ti, Mn, Fe, Co, Ni) show a large variety of structures and physical properties. Among them is $BaTiO_3$ (BTO), one of the most investigated and used perovskites. In a BTO film on Pt(111), the first oxide quasicrystal was discovered. Herein, by means of first-principle methods, the cubic and hexagonal phases of bulk $BaFeO_3$ (BFO) are investigated. Both phases show ferromagnetic order. Monolayers and double layers of BFO are studied on a Pt(111) surface. The double-layer configuration of the cubic and hexagonal phases is structurally inequivalent but both double-layer films show antiferromagnetic order. In analogy to the BTO quasicrystal approximant structure on Pt(111), a corresponding BFO structure is investigated. The Fe atoms are surrounded by three oxygen atoms and the resulting FeO_3 units are separated by barium atoms with the total stoichiometry $Ba_5Fe_4O_{12}$.

1. Introduction

The discovery of the first oxide quasicrystal (OQC) by Förster et al.[1] formed in a $BaTiO_3$ (BTO) layer on the Pt(111) surface was practically a change of paradigm. The BTO quasicrystal has dodecagonal symmetry and is formed by squares, triangles, and 30° rhombs as parts of a Niizeki–Gähler tiling.[2–4] By the same group, it was shown later that $SrTiO_3$ also forms an oxide quasicrystal on the Pt(111) surface.[5] Until this discovery, quasicrystals in one, two, or three dimensions are found mainly in intermetallic systems[6] or are fabricated artificially, for instance, for applications in photonics.[7–9]

Quasicrystal approximant structures (QCAs) are periodic arrangements which are closely related to the local structure of the quasicrystal itself.[10] Thus, such a structure can serve as a starting point for a detailed investigation of the local structure of the quasicrystal. Due to its lattice periodicity, QCAs can be studied theoretically by means of standard methods based on density functional theory (DFT).

An approximant structure related to the BTO quasicrystal was investigated by Förster et al.[11] by means of a combination of experimental techniques and first-principle calculations. The structure was identified as the $3^2.4.3.4$ Archimedian tiling, already described by Kepler in 1619. Atomic positions in this tiling have been identified by Förster et al.[11] Experimentally, a rich variety of different perovskite-like oxides with different crystal structures are known, combining an alkaline earth metal (A) such as Ca, Sr, and Ba and a transition metal (B) such as Mn, Fe, Co, and Ni.[12–26] BTO and $SrTiO_3$ form oxide quasicrystalline or quasicrystalline approximant structures on Pt(111). We expect that, in between the variety of the ABO_3 structures, other potential candidates for OQCs can be found.

Because neither BTO nor $SrTiO_3$ is magnetic, it is interesting to ask the question whether other perovskites-like ABO_3 oxides having magnetic or other interesting properties would be candidates to form OQCs or corresponding approximant structures.

Of special interest in this context are the magnetic alkaline-earth ferrates $CaFeO_3$, $SrFeO_3$, and $BaFeO_3$ (BFO), because of a high spin state of Fe. The oxide $CaFeO_3$ is insulating below 290 K.[27] Fe appears as Fe^{3+} and Fe^{5+} in this oxide.[14] In contrast, $SrFeO_3$ contains Fe in the high spin state Fe^{4+} and shows metallic conductivity even below $T_N = 134$ K, i.e., in an antiferromagnetic (AFM) state.[28] Below T_N, it shows a G-type helical spin order.[19]

$BaFeO_{3-\delta}$ adopts different phases depending on the oxygen deficiency as studied in detail by Mori et al.[29,30] The hexagonal phase exists in a wide range of oxygen content and is known for a long time.[29] The hexagonal modification of $BaFeO_{3-\delta}$ is an excellent example of a magnetic perovskite-like oxide with a

Dr. W. A. Adeagbo, Dr. I. V. Maznichenko, H. Ben Hamed, Dr. I. Mertig, Dr. W. Hergert
Institute of Physics
Martin Luther University Halle-Wittenberg
Von-Seckendorff-Platz 1, 06120 Halle (Saale), Germany
E-mail: waheed.adeagbo@physik.uni-halle.de

Dr. A. Ernst
Institute for Theoretical Physics
Johannes Kepler University Linz
Altenberger Straße 69, 4040 Linz, Austria

Dr. A. Ernst
Max Planck Institute of Microstructure Physics
Weinberg 2, 06120 Halle (Saale), Germany

The ORCID identification number(s) for the author(s) of this article can be found under https://doi.org/10.1002/pssb.201900649.

DOI: 10.1002/pssb.201900649

charge disproportion of Fe^{4+}. A change of the Fe^{4+} concentration was experimentally found to exist around 170 K.

The stoichiometric cubic perovskite phase was synthesized only recently by Hayashi et al.[24] The cubic BFO also favors Fe^{4+} and is characterized by an A-type spin spiral below 111 K.[24] A small magnetic field of 0.3 T is enough to destroy the spin spiral and to stabilize ferromagnetic (FM) order with a magnetic moment of 3.5 μ_B.[24]

In a series of articles, the electronic and magnetic structures of cubic BFO are investigated.[31–33] A thorough analysis of the electronic and magnetic properties and the role of oxygen vacancies as well as the Fe oxidation state in cubic BFO was given in a previous study,[31] but detailed first-principle calculations of hexagonal BFO are not available, to the best of our knowledge.

With respect to Pt(111) as a substrate, BFO has a very good lattice match and also robust magnetic properties. Thus, new interesting features could appear in thin BFO layers on Pt(111) and possibly in a corresponding quasicrystal or its approximant structure.

This article is organized as follows. After a short introduction to the crystal structures, forming the basis of the investigation, the computational methods are introduced. Afterwards, bulk properties of the cubic and hexagonal phase of BFO are studied. In preparation for the discussion of the QCA with its large unit cell, monolayer and bilayer structures of BFO on Pt(111) with the usual small unit cells are considered. Finally, the BFO approximant structure will be constructed and compared with the corresponding BTO structure on Pt(111). A conclusion will end this article.

2. Crystal Structures and Computational Details

2.1. Crystal Structures

At room temperature, BTO, forming a quasicrystalline structure on Pt(111), is stable in the tetragonal ferroelectric phase. It also exists as a 6H hexagonal polymorph. This phase occurs at 1430 °C in air.[34,35] The hexagonal phase can be stabilized down to room temperature by a small amount of transition metal atoms.[36–38] Interestingly, BFO also appears in both phases.

Figure 1 shows the cubic perovskite and the 6H hexagonal structure of BFO. The cubic phase is shown along the ⟨111⟩ direction for ease of comparison with hexagonal setting. Both cells contain 30 atoms and differ by the stacking sequence.

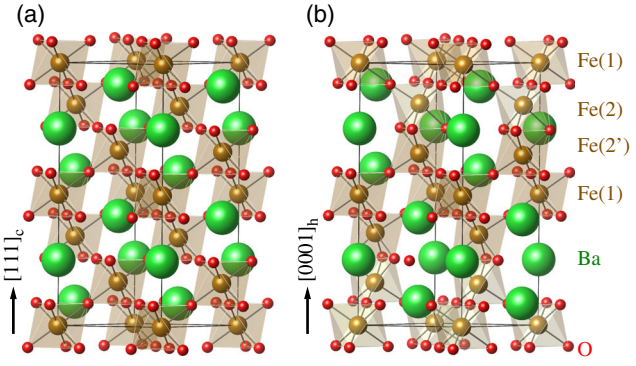

Figure 1. Phases of BFO. a) (3C) cubic phase, b) (6H) hexagonal phase (golden: Fe, green: Ba, red: O).

In the cubic phase, there exists only one type of site per atomic species, but in the 6H modification, all three atomic species occupy two different sites. The cubic phase in Figure 1a is characterized by exclusively corner-sharing octahedra. In *h*-BFO (Figure 1b), appear corner-sharing but also face-sharing octahedra. The Fe(1) atoms are located in the center of the corner-sharing octahedra, but the Fe(2) atoms occupy the center of the face-sharing and corner-sharing octahedra. Fe(2) and Fe(2′) are structurally equivalent, but it is important to distinguish the layers in the discussion of the magnetic properties. The O(1) atoms are located in the layers between the Fe(2) and the O(2) atoms are at the vertices of the corner-sharing octahedra. Ba and O appearing in two types in *h*-BFO are not of primary interest in the following consideration. Thus, those atom types are not marked in the figure explicitly. Although the 6H structure is stabilized by an oxygen deficiency at the O(1) sites,[30] the ideal structure is assumed in the following investigation, if not mentioned otherwise.

It is immediately obvious from Figure 1 that both structures possess different stacking sequences. Therefore, this has to be considered in a systematic investigation of thin layers.

2.2. Computational Details

The calculations are based on DFT and are performed by the plane-wave pseudopotential method as implemented in the Vienna Ab Initio Simulation Package (VASP)[39,40] and a self-consistent Green function method within multiple scattering theory.[41–43]

2.2.1. VASP Calculations

The Perdew–Wang 91 (PW91) generalized gradient approximation (GGA)[44] was used to describe electron–electron exchange and correlation interactions. By means of the projector augmented wave (PAW) method[45,46] with the following valence state configurations (Fe[$3d^7 4s^1$], Ba[$5s^2 5p^6 6s^2$], and O[$2s^2 2p^4$]), the valence electrons are treated self-consistently.

The kinetic energy cutoff for the plane waves is set to 400 eV. All calculations were done in spin-polarized mode. The structural relaxation is performed until the interatomic forces converged below the threshold value of 25 meV Å^{-1}. The total energy, the density of states (DOS), and other bulk-related properties are computed at the Γ-centered $6 \times 6 \times 8$ Monkhorst-Pack *k*-point mesh. For layer calculations, a Γ-centered $6 \times 6 \times 1$ mesh was used. Due to the size of the unit cell, the Γ-point approximation was used for the discussion of the approximant structure on Pt(111).

The problem of standard exchange correlation functionals in DFT in accounting for the strong correlations caused by localized d electrons can be partially fixed in the framework of the DFT + U approach.[47,48] For iron oxides, correlations of the 3d electrons of Fe have to be corrected. A Hubbard-U value between 3.0 and 5.0 eV[49] is typically recommended for Fe to scan the whole electronic properties of Fe in oxides. Best overall agreement of structural, magnetic, and electronic properties of α-Fe_2O_3 with experimental data is obtained for $U = 4$ eV in

previous studies.[50,51] Also, $BiFeO_3$ ($U = 4$ eV)[49] and $ZnFe_2O_4$ ($U = 3.5$ eV)[52] fit into this scheme. Several first-principle calculations on cubic BFO[32,53,54] also come to the conclusion that $U = 4$ eV is appropriate in case of BFO. Thus, we have also used $U = 4$ eV for the Fe 3d states corrected in the GGA + U framework according to the scheme of Dudarev as implemented in VASP code.[39,40,55]

The structural parameters such as the lattice constants and atom coordinates were optimized via minimizing the total energy. We use the four-parameter Birch–Murnaghan equation of state to fit the volume dependence of the total energy to obtain the bulk modulus (B_0) and its pressure derivative (B') at zero pressure.[56] Layer structures are modeled with a four-layer thick Pt substrate. The layers are separated by a 22 Å-thick vacuum layer to prevent any surface–surface interaction.

2.2.2. Green's Function Method

A first-principle Green's function method[41,57] based on multiple scattering theory within DFT GGA was used to study magnetic properties in detail. A maximum angular momentum of $l_{max} = 3$ was used to consider the nonsphericity of charge density and crystal potential. The influence of oxygen vacancies was described using a coherent potential approximation[58] as it is implemented within the multiple scattering theory.[59] The magnetic interaction was estimated using the magnetic force theorem, in which exchange parameters entering the Heisenberg model are calculated from the energy cost due to an infinitesimal rotation of magnetic moments.[60]

3. Results and Discussion

We start the discussion with a detailed analysis of both bulk phases discussed in Section 2.1. Finally, the BFO QCA, a periodic monolayer structure on Pt(111), is studied. Thus, to gain some insight in the complex relaxations of BFO on Pt(111), a BFO monolayer and BFO bilayers are considered. Due to the different stacking in cubic and hexagonal bulk crystals, bilayers with two different structures are investigated. Structural, mechanical, and magnetic properties of both bulk phases are discussed in Section 3.1. The results for the layer structures (Section 3.2) and the approximant structure (Section 3.3) are presented afterwards.

3.1. Bulk Properties

It was already mentioned that small magnetic fields destroy the spin spiral and stabilize FM order.[24] Thus, spin spirals are not included in the following investigation. A series of magnetic structures are assumed to find the ground-state magnetic structure. Due to the two inequivalent Fe positions in the 6H modification, more magnetically inequivalent structures can be constructed than for the cubic phase.

3.1.1. Cubic Structure

The magnetic structures considered for the cubic phase are shown in **Figure 2**. In addition to the FM structure, three AFM configurations, designated as usual as A-type, C-type, and G-type, are considered. (For more details, see ref. [61]). Structural relaxations have been performed without and with correlation corrections. They differ only slightly. Thus, only the results calculated in the GGA + U framework are presented.

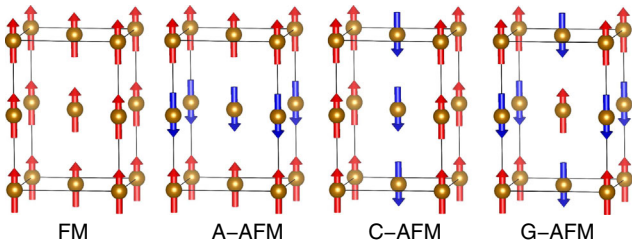

Figure 2. The magnetic configurations considered for cubic BFO: FM structure and three antiferromangetic configurations (A-AFM, C-AFM, G-AFM). Only the Fe atoms are shown for clarity.

The results shown in **Table 1** confirm that the FM structure has the lowest energy of the considered magnetic structures in our calculation. Except for the energy differences between the magnetic structures, all self-consistently calculated properties are nearly equal. A little increase in the lattice constant a going from FM to G-AFM is connected with a decrease in B_0 and B'.

A good agreement is not only achieved with experiment but also with other calculations. Cherair et al.[32] used the ABINIT code, whereas Wien2K was applied by Noura.[33] In both calculations, correlation corrections are performed in the LDA + U framework.

3.1.2. Hexagonal Structure

The hexagonal phase of Figure 1b is in the focus now. The cubic structure in hexagonal setting shown in Figure 1a is considered for comparison. **Figure 3** shows the magnetic structures considered for the hexagonal phase. As shown in Figure 1b, Fe occupies two inequivalent sites, Fe(1) and Fe(2). In addition to the FM phase, we not only consider a configuration, in which each Fe sublattice is FM, but also the two Fe sublattices which are antiferromagnetically coupled to each other. This results in a

Table 1. Calculated properties of cubic BFO configurations and comparison with experimental results and other calculations. Energy differences per formula unit ΔE are related to FM structure (α—lattice constant, m_{Fe}—magnetic moment of Fe, B_0—bulk modulus, B'—pressure derivative of bulk modulus).

Structure	ΔE [meV]	α [Å]	m_{Fe} [μ_B]	B_0 [GPa]	B'
FM	0	4.013	3.81	119.59	4.79
A-AFM	177	4.015	3.78	117.99	4.78
C-AFM	226	4.021	3.80	116.44	4.67
G-AFM	297	4.033	3.86	113.23	4.41
Exp.[24]	–	3.971	3.5	–	–
Calc.[32]	–	3.990	4.01	124.70	4.59
Calc.[33]	–	4.026	3.97	116.00	4.50
Calc.[62]	–	4.021	3.87	–	–

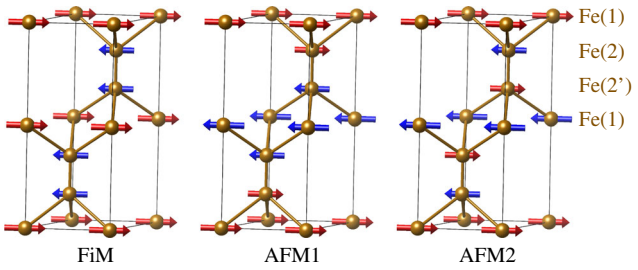

Figure 3. Magnetic configurations considered for the hexagonal structure of BFO shown in Figure 1. Only the Fe atoms are shown for clarity.

ferrimagnetic solution (FiM in Figure 3). In the two AFM structures AFM1 and AFM2, both sublattices reveal an AFM coupling with a ferromagnetic (AFM1) or antiferromagnetic (AFM2) coupling between the sublattices.

First, we compare the calculated lattice structure with experimental results. The lattice constants for the studied magnetic structures differ only slightly as for the cubic case. By means of GGA + U, we find $a = 5.690$ Å and a c/a ratio of $c/a = 2.428$. The structural data given by Mori et al.[30] for lattice constant $a = 53\,674$ Å and $c = 13.930$ Å ($c/a = 2.455$) are in good agreement with the calculation. It should be mentioned that Mori's data belong to a crystal with oxygen deficiency ($BaFeO_{2.913}$).

The results of all calculations are shown in **Table 2**. All energies are related to the FM state of the 6H hexagonal phase BFO. The energy difference between FM and AFM1 is small, as for FiM and AFM2. It follows that the layers Fe(2) and Fe(2) are magnetically coupled very weakly. Therefore, it is necessary to study the effect of oxygen vacancies located between them.

The coupling constants for the hexagonal structure are calculated by means of the Green's function method. The oxygen vacancies between Fe(2) and Fe(2′) are described by the coherent potential approximation. As expected, the corner-shared octahedra are coupled strongly ferromagnetically, as it was found in *c*-BFO.[31] The coupling between Fe(1) and Fe(2) (J_{12}) is strongly positive in both ideal structures and in $BaFeO_{2.913}$. An oxygen atom is located between Fe(1) and Fe(2), which is typical in a perovskite structure and results in the double exchange coupling between the magnetic moments. In contrast, the coupling between two Fe(2) atoms is AFM (J_{22} is negative). The coupling constants J_{11}, J_{12}, and J_{22} as a function of distance in both BFO and $BaFeO_{2.913}$ are shown in **Figure 4**. The coupling constant J_{22} is responsible for a tendency to AFM ordering in the Fe(2) sublattice in different layers. Other J's except at distance 7.8 Å are negligible small.

Table 2. Calculated magnetic properties of the structures in Figure 3. The energy of the FM hexagonal phase per formula unit is taken as reference.

Structure	ΔE [meV]	$m_{Fe(1)}$ [μ_B]	$m_{Fe(2)}$ [μ_B]
FM	0	3.99	3.58
FiM	86.9	4.10	−3.35
AFM1	0.7	3.99	3.56
AFM2	87.0	4.11	3.32

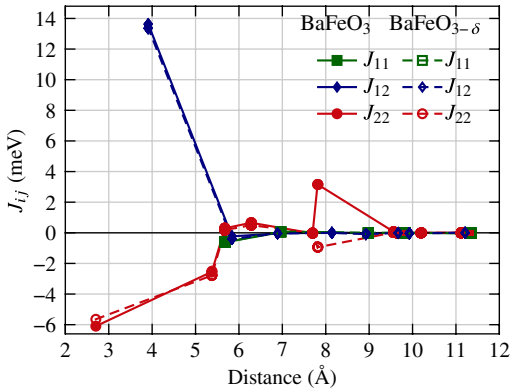

Figure 4. Exchange coupling constants, calculated for the 6H hexagonal structure $BaFeO_{3-\delta}$, with $\delta = 0$, the absence of oxygen vacancy (solid lines) and $\delta = 0.087$, the presence of oxygen vacancy, V_O (dashed lines).

Due to this fact, we expect for single layers no magnetic coupling at all. However, the presence of a vacancy is crucial for the magnetic interaction between the moments at 7.8 Å. Although without vacancies the interaction is strongly positive, in the presence of a vacancy, it becomes negative. The reason for this behavior is an increase in *d*–*d* hybridization between the Fe atoms due to the absence of the oxygen atom. This enhancement of the AFM interaction between Fe(2) layers leads to a stabilization of the AFM configuration AFM1 (Figure 3).

3.2. Layer Structures on Pt(111)

The periodic layer structures discussed here are cut out of the crystal structures shown in Figure 1 perpendicular to the *c*-axis. Monolayers from both *c*-BFO and *h*-BFO structures are equivalent. Different stacking sequences follow for bilayers. Due to the inequivalent iron sites in *h*-BFO, it is interesting to study the relaxation on the Pt(111) surface and the magnetic properties of those layer systems in comparison with the bulk structures and the QCA.

A stacking of an Fe(1) and the consecutive Fe(2) plane in the hexagonal structure is equivalent to the stacking of two layers in the cubic model of Figure 1. Such a bilayer will be named stacking sequence 1 (SS1). A different stacking follows, if we cut out two consecutive Fe(2) planes from the hexagonal structure. This will be termed stacking sequence 2 (SS2). The stacking SS2 of two monolayers does not appear in the cubic model.

In the following calculations, the unit cell of the added BFO layers is fixed to the Pt surface such that the Ba atoms are either in registry with the hollow sites or on top of Pt. The calculated starting configurations with minimum energy before relaxation are shown in **Figure 5**, **6**, and **7**. The Fe surface termination is always energetically preferred to the BaO termination. This is in agreement with the experimental growth pattern of thin film of BTO on Pt (111).[63] A Ti surface termination is preferred in this case. In case of one monolayer and two monolayers of SS2 stacking Ba resides at the hollow side, but for the SS1 case on top of Pt. All inner coordinates are allowed to relax. What follows is a qualitative discussion of the relaxations. We avoided to present large tables of the detailed relaxation data.

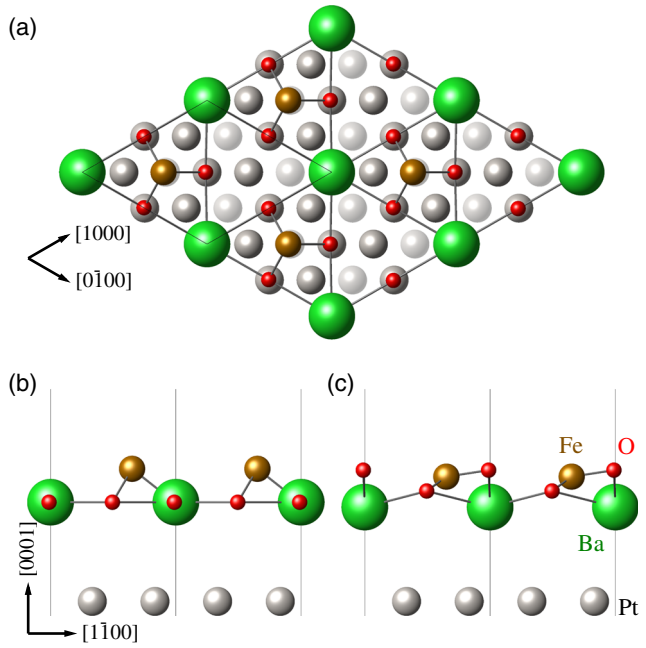

Figure 5. One-monolayer BFO on Pt(111). a) Top view of the unrelaxed structure; b) side view of the unrelaxed structure; c) side view of the relaxed structure.

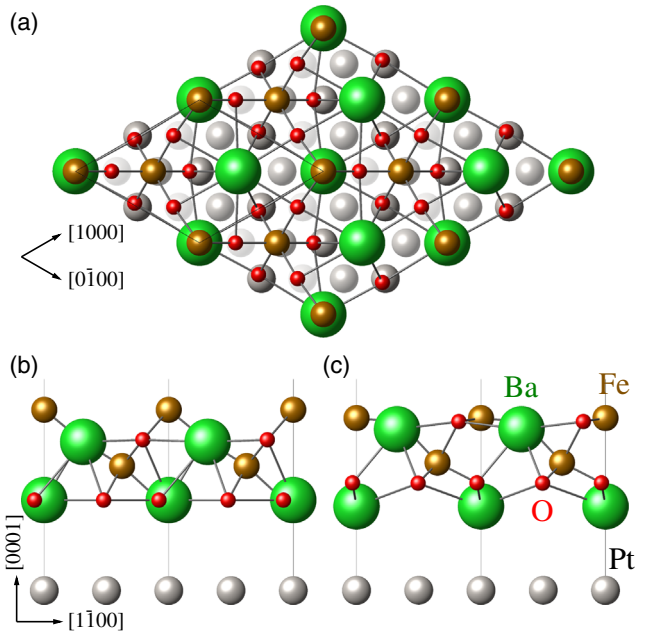

Figure 6. Two-monolayer BFO on Pt(111) in SS1 stacking. a) Top view of the unrelaxed structure; b) side view of the unrelaxed structure; c) side view of the relaxed structure.

3.2.1. Monolayer

Figure 5 shows the relaxation of the monolayer. In the unrelaxed structure, all atoms are located in hollow sites. The relaxation is characterized by a minimal inward relaxation of Ba and also an outward relaxation of oxygen toward the Fe atoms. The Fe atoms shift out of the symmetric hollow site position. FM and AFM arrangements of the Fe moments have been tested. Both structures differ in total energy by less than 1 meV. The magnetic moment is 2.14 μ_B, practically half of the typical bulk values, shown in Table 1 and 2.

3.2.2. Bilayers

Figure 6 and 7 show the bilayers in the two different stacking sequences on Pt(111). Differences in the relaxations are obvious. Ba relaxations in the interface layer for SS1 stacking is again minimal, but a stronger inward relaxation of Ba at the interface for SS2 stacking is obtained. The Ba atoms in the surface layers show an outward relaxation. From the side views of Figure 6b and 7b, it can be seen that oxygen is located in the Ba planes without relaxation. Afer relaxation, practically all O atoms move outward. The Fe atoms in the surface layer are also affected by relaxation. They move toward the Pt surface. For the SS1 stacking that leads to a surface plane containing practically all types of atoms (Figure 6c). The distance of the Fe atoms in the bilayer of the SS2 stacking corresponds to its bulk value. In SS2, stacking a partial oxygen termination is obtained, as shown in Figure 7c.

An FM and an antiferomagnetic (AFM) coupling of the layers in the bilayer system was investigated. The results for the magnetic moments are compiled in **Table 3**. In the SS1 stacking, the AFM structure is preferred with respect to the FM structure by an energy difference of 34 meV. The Pt atoms in the Pt surface layer are partially polarized by the interface Fe atoms. Thus, the Fe moment at the interface is lower than in the surface layer. The SS2 stacking sequence also leads to a stable AFM coupling

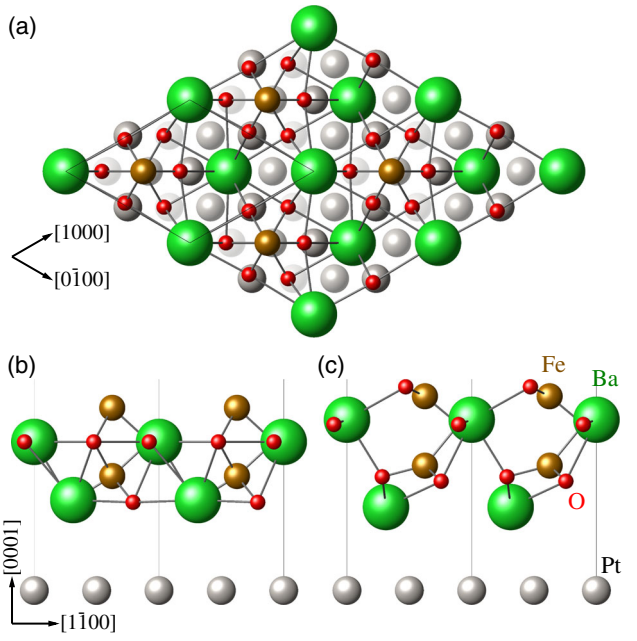

Figure 7. Two-monolayer BFO on Pt(111) in SS2 stacking. a) Top view of the unrelaxed structure; b) side view of the unrelaxed structure; c) side view of the relaxed structure.

Table 3. Calculated magnetic moments of Fe and energy differences ΔE related to FM structure in layer systems on the Pt(111) surface.

Structure	ΔE [meV]	m_{Fe} [μ_B]	
		Interface	Surface
ML		2.14	
ML SS1 FM	0	2.40	2.74
ML SS1 AFM	−34	−2.42	2.63
ML SS2 FM	0	1.92	3.04
ML SS2 AFM	−195	−1.88	2.23
Approximant		3.30	

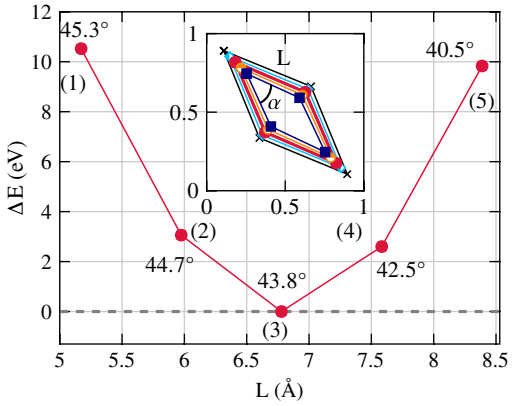

Figure 9. Energy differences between structures of different rhombus sizes for the free-standing approximant structure.

lower in energy by 195 meV compared with the FM order. Also, in this case, the moment of the interface Fe atoms is decreased, but the moment of the surface Fe atoms is a bit higher than in the SS1 case. The enhanced superficial magnetization found for all our considered surface terminations in Table 2 are peculiar for undercoordinated magnetic nanoparticles of reduced sizes at the surfaces, as reported for perovskite-like $MnTiO_3$[64] and the spinel structure, Co_3O_4.[65,66] It is known that the enhancement of surface magnetism arises because of band narrowing at the surface due to decrease in the coordination number and symmetry.[67–70] Such undercoordination or reduced symmetry play an important role in the magnetic ordering of the films compared with the bulk.

3.3. BFO Approximant Structure

For the construction of the QCA, the same procedure was applied and that was already successfully used in case of the BTO OCQ.[11] First, a 13.9 Å × 14.4 Å surface supercell of Pt is constructed based on the Pt lattice constant of $a = 3.92$ Å. The formal stoichiometry of the BTO case is transferred to the new system, i.e., $Ba_5Fe_4O_{12}$ is used. In the first step, the size of the Fe rhombi in a free-standing layer is varied and the Ba and O positions are relaxed. **Figure 8** shows the corresponding structures. The procedure is used to find the optimal rhombus size, i.e., the structure with minimal energy. This is structure (3) of Figure 8, as shown from the energies in **Figure 9**. The most stable rhombus has a side length of $L = 6.78$ Å and an angle $\alpha = 43.77°$. Although in this approximation the approximant is substrate unsupported, all the atoms relax in the 2D plane. No vertical relaxation is observed.

The relaxed structure shown in Figure 8(3) is used as the starting structure for further relaxation on top of the Pt(111) surface. The final relaxations in this structure with a large unit cell are different from those discussed for one monolayer, as shown in Figure 5. The whole monolayer relaxes away from the Pt surface. The buckling in the monolayer (Figure 5c) disappears in the QCA, i.e., Fe and Ba atoms are in plane. In **Figure 10**, not only the magnetization density in the approximant structure is plotted, but also the structural information can be readout of the figure. The monolayer case is characterized by an outward relaxation of the oxygen atoms. Figure 10b,c reveals that all O atoms can be divided into two types. One part of the O atoms is located slightly over the Ba—Fe plane (average Fe—O bond length 1.72 Å), whereas the rest is located in this plane and is bound to the Pt surface (average Fe—O bond length 1.93 Å). Each Fe atom is bound to three oxygen atoms in a FeO_3 complex. The relaxation for the BFO approximant structure are quite similar to BTO.[11]

The magnetization density in Figure 10 is shown for an FM ordering of the Fe atoms. Other magnetic states are possible because due to the large distance between Fe atoms in the approximant, the spin polarization can be switched separately for each atom. The shortest distance between Fe atoms in the approximant is 5.84 Å, which is comparable with in-plane

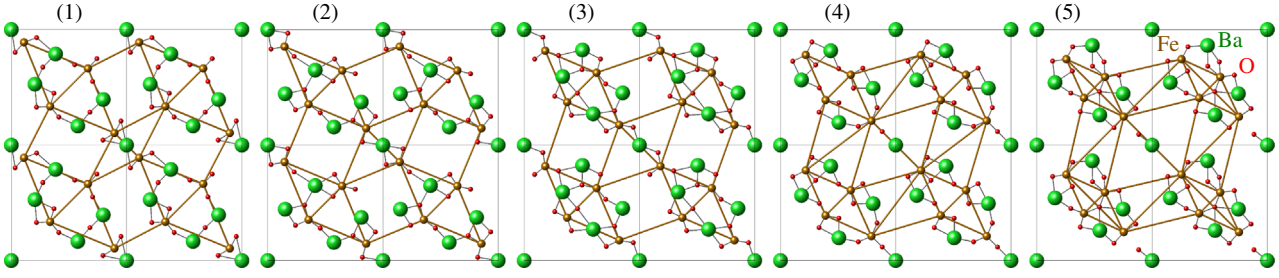

Figure 8. Relaxation of the rhombi forming the free-standing approximant structures of different free-standing layers. A series of rhombi of different dimensions with four Fe positions were constructed. The opposite pairs of Fe positions are equivalent by symmetry. Each Fe atom is saturated arbitrarily with three oxygen atoms, whereas four Ba atoms are distributed on the side of a rhombus and the fifth Ba placed at the origin of the square. The exact positions of Ba and O are then energy minimized in (1)–(5).

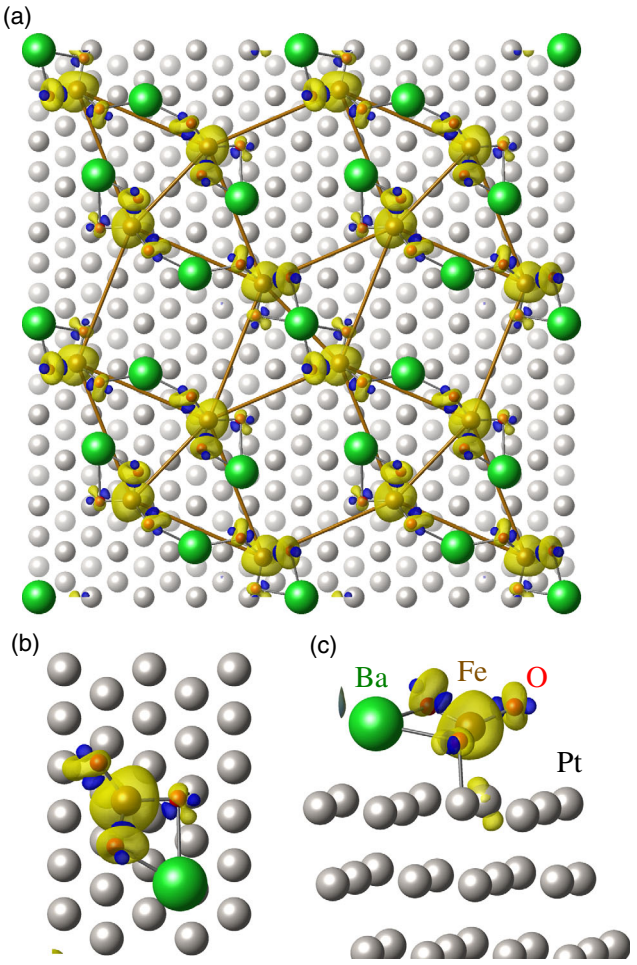

Figure 10. 3D magnetization density plot of the approximant structure of BFO on Pt(111). The isodensity value is set to $\pm 0.005\,\mu_B$ Å^{-3}, with positive isodensity (spin-up) in yellow and negative isodensity (spin-down) in blue. a) Top view; b) top view of a characteristic building block; c) side view of the block shown in part (b).

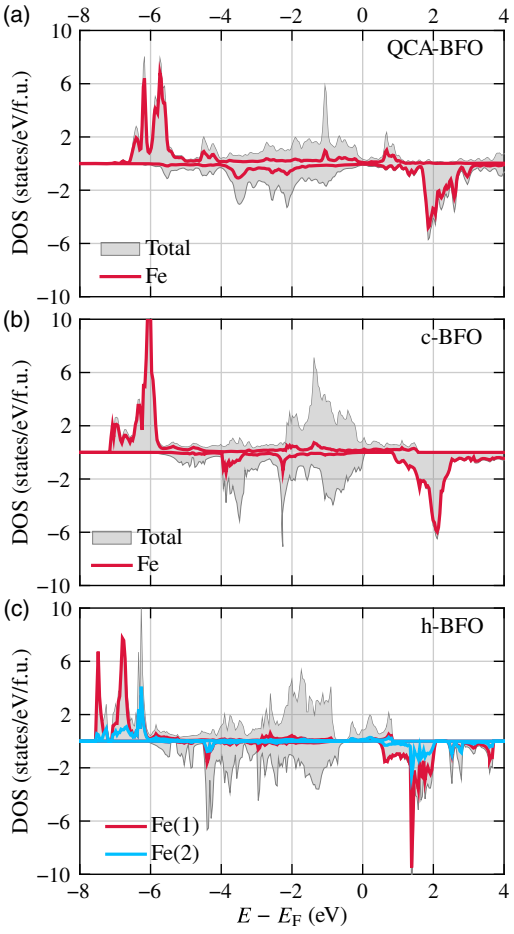

Figure 11. The total and partial density of states (PDOS) for BFO unit in a) the cubic, b) the 6H hexagonal, and c) the approximant structure are compared. The DOS has been shifted such that the Fermi energy is at zero in the plots.

distances in *h*-BFO structure. Such Fe atoms do not interact directly, as shown in Figure 4. A magnetic moment of $3.3\,\mu_B$ is obtained for iron, a bit larger than for the layer systems discussed before. A strong polarization of the O atoms and the polarization of Pt atoms underneath can also be seen in Figure 10b,c.

The induced moments on upper oxygen atoms are $0.15\,\mu_B$, whereas the total magnetic moment induced on an oxygen atom bound to Fe and Pt is ten times smaller. Pt atoms which are sitting directly under Fe atoms become a little magnetic with induced magnetic moment $0.1\,\mu_B$, whereas other Pt and Ba atoms do not show any evidence of spin polarization.

The calculated total and partial DOS for one unit cell of the approximant structure is compared with the DOS of cubic and 6H hexagonal BFO in **Figure 11**. The shape of Fe 3d states around the Fermi level in the approximant structure in Figure 11a is most similar to the shape of the DOS of the Fe atoms in the *c*-BFO structure in Figure 11b, despite the fact that the value of moment of the atom Fe in the approximant is closer to the value of the moment of a Fe(2) atom in *h*-BFO than for a Fe atom in the cubic structure.

The DOSs of *c*-BFO and *h*-BFO in Figure 11b,c are calculated in the FM state with $U = 4$ eV. The half-metallic character is obvious in both cases and completely absent in the case of the QCA structure shown in Figure 11a. It should be noted that in the GGA calculations (not shown here for Figure 11b,c), both *c*-BFO and *h*-BFO are metallic. Because the magnetic moments of the Fe atoms are caused by the Fe 3d electrons, only the Fe 3d partial DOS are shown in Figure 11a–c. All figures reveal that the states near the Fermi energy are mainly from O 2p states. Due to the reduced symmetry, the d-DOS of both Fe species in *h*-BFO is different, and also the Fe of the QCA. The gap in the minority channel of the hexagonal phase is larger than that in the cubic phase and completely zero in the case of the QCA.

4. Conclusions

A comparative first-principle study of bulk BFO in cubic and hexagonal phases was performed. The real structure relaxations

for a monolayer and bilayers with different stacking sequences are discussed in detail. The stacking sequence has strong influence on the relaxation. No preference between FM and AFM order can be found for the monolayer, but the layer AFM state is stabilized for the bilayers, independent on the stacking sequence. The relaxation of the BFO quasicrystal approximant structure on Pt(111) is similar to the corresponding BTO structure, but the BFO structure remains magnetic on Pt(111) with high magnetic moments of Fe.

If this approximant structure or the corresponding quasicrystal could be prepared, the magnetism in the quasicrystal layer would open a new field in OQC research.

Acknowledgements

This work was funded by the Deutsche Forschungsgemeinschaft (DFG, German Research Foundation) Projektnummer 31047526, SFB 762, project A4.

Structural plots are prepared by means of VESTA 3 [cf. K. Momma, F. Izumi, *J. Appl. Crystallogr.* **2011**, *44*, 1272].

Conflict of Interest

The authors declare no conflict of interest.

Keywords

density functional theory, magnetism, oxide quasicrystals, perovskites

Received: October 8, 2019
Revised: January 30, 2020
Published online: April 6, 2020

[1] S. Förster, K. Meinel, R. Hammer, M. Trautmann, W. Widdra, *Nature* **2013**, *502*, 215.
[2] N. Niizeki, H. Mitani, *J. Phys. A, Math. Gen.* **1987**, *20*, L405.
[3] F. Gähler, in *Proc. of the ILL/CODEST Workshop*, World Scientific, Singapore **1988**, p. 13.
[4] S. Schenk, E. M. Zollner, O. Krahn, B. Schreck, R. Hammer, S. Förster, W. Widdra, *Acta Crystallogr. Sect. A* **2019**, *75*, 307.
[5] S. Schenk, S. Förster, K. Meinel, R. Hammer, B. Leibundgut, M. Paleschke, J. Pantzer, C. Dresler, F. O. Schumann, W. Widdra, *J. Phys.: Condens. Matter* **2017**, *29*, 134002.
[6] W. Steurer, S. Deloudi, *Crystallography of Quasicrystals – Concepts, Methods and Structures*, Springer, Heidelberg **2009**.
[7] Z. V. Vardeny, A. Nahata, A. Agrawal, *Nat. Photonics* **2013**, *7*, 177.
[8] L. Dal Negro, S. Boriskina, *Laser Photonics Rev.* **2012**, *6*, 178.
[9] A. Poddubny, E. Ivchenko, *Physica E, Low Dimens. Syst. Nanostruct.* **2010**, *42*, 1871.
[10] A. I. Goldman, R. F. Kelton, *Rev. Mod. Phys.* **1993**, *65*, 213.
[11] S. Förster, M. Trautmann, S. Roy, W. A. Adeagbo, E. M. Zollner, R. Hammer, F. O. Schumann, K. Meinel, S. K. Nayak, K. Mohseni, W. Hergert, H. L. Meyerheim, W. Widdra, *Phys. Rev. Lett.* **2016**, *117*, 095501.
[12] S. V. Náray-Szabó, *Naturwissenschaften* **1943**, *31*, 202.
[13] K. Poeppelmeier, M. Leonowicz, J. Scanlon, J. Longo, W. Yelon, *J. Solid State Chem.* **1982**, *45*, 71.
[14] M. Takano, N. Nakanishi, Y. Takeda, S. Naka, T. Takada, *Mater. Res. Bull.* **1977**, *12*, 923.
[15] T. Osaka, H. Takahashi, H. Sagayama, Y. Yamasaki, S. Ishiwata, *Phys. Rev. B* **2017**, *95*, 224440.
[16] A. Jain, S. P. Ong, G. Hautier, W. Chen, W. D. Richards, S. Dacek, S. Cholia, D. Gunter, D. Skinner, G. Ceder, K. A. Persson, *APL Mater.* **2013**, *1*, 011002.
[17] K. A. Müller, H. Burkard, *Phys. Rev. B* **1979**, *19*, 3593.
[18] H. Taguchi, A. Shimizu, M. Nagao, H. Kido, *J. Ceram. Soc. Jpn.* **2007**, *115*, 77.
[19] T. Takeda, Y. Yamaguchi, H. Watanabe, *J. Phys. Soc. Jpn.* **1972**, *33*, 967.
[20] Y. Long, Y. Kaneko, S. Ishiwata, Y. Taguchi, Y. Tokura, *J. Phys.: Condens. Matter* **2011**, *23*, 245601.
[21] Y. Takeda, T. Hashino, H. Miyamoto, F. Kanamaru, S. Kume, M. Koizumi, *J. Inorg. Nucl. Chem.* **1972**, *34*, 1599.
[22] H. T. Evans, *Acta Crystallogr.* **1951**, *4*, 377.
[23] T. Negas, R. Roth, *J. Solid State Chem.* **1971**, *3*, 323.
[24] N. Hayashi, T. Yamamoto, H. Kageyama, M. Nishi, Y. Watanabe, T. Kawakami, Y. Matsushita, A. Fujimori, M. Takano, *Angew. Chem. Int. Ed.* **2011**, *50*, 12547.
[25] H. Taguchi, Y. Takeda, F. Kanamaru, M. Shimada, M. Koizumi, *Acta Crystallogr. Sect. B* **1977**, *33*, 1298.
[26] Y. Takeda, F. Kanamura, M. Shimada, M. Koizumi, *Acta Crystallogr. Sect. B* **1976**, *32*, 2464.
[27] S. Kawasaki, M. Takano, R. Kanno, T. Takeda, A. Fujimori, *J. Phys. Soc. Jpn.* **1998**, *67*, 1529.
[28] N. Hayashi, T. Terashima, M. Takano, *J. Mater. Chem.* **2001**, *11*, 2235.
[29] S. Mori, *J. Am. Ceram. Soc.* **1966**, *49*, 600.
[30] K. Mori, T. Kamiyama, H. Kobayashi, K. Oikawa, T. Otomo, S. Ikeda, *J. Phys. Soc. Jpn.* **2003**, *72*, 2024.
[31] I. V. Maznichenko, S. Ostanin, L. V. Bekenov, V. N. Antonov, I. Mertig, A. Ernst, *Phys. Rev. B* **2016**, *93*, 024411.
[32] I. Cherair, E. Bousquet, M. M. Schmitt, N. Iles, A. Kellou, *J. Phys.: Condens. Matter* **2018**, *30*, 255701.
[33] H. Noura, *Superlattices Microstruct.* **2014**, *76*, 425.
[34] K. W. Kirby, B. A. Wechsler, *J. Am. Ceram. Soc.* **1991**, *74*, 1841.
[35] D. Kolar, U. Kunaver, A. Rečnik, *Phys. Status Solidi A* **1998**, *166*, 219.
[36] G. M. Keith, M. J. Rampling, K. Sarma, N. M. Alford, D. C. Sinclair, *J. Eur. Ceram. Soc.* **2004**, *24*, 1721.
[37] R. Böttcher, H. T. Langhammer, T. Müller, H. P. Abicht, *J. Phys.: Condens. Matter* **2008**, *20*, 505209.
[38] S. K. Nayak, W. A. Adeagbo, H. T. Langhammer, W. Hergert, T. Müller, R. Böttcher, *Phys. Status Solidi RRL* **2014**, *8*, 527.
[39] G. Kresse, J. Furthmüller, *Comput. Mater. Sci.* **1996**, *6*, 15.
[40] G. Kresse, J. Furthmüller, *Phys. Rev. B* **1996**, *54*, 11169.
[41] A. Ernst, Multiple-Scattering Theory: New Developments and Applications, Kumulative Habilitationsschrift, Martin-Luther-Universität Halle-Wittenberg, Halle, Germany **2007**.
[42] M. Geilhufe, S. Achilles, M. A. Köbis, M. Arnold, I. Mertig, W. Hergert, A. Ernst, *J. Phys.: Condens. Matter* **2015**, *27*, 435202.
[43] M. Hoffmann, A. Ernst, W. Hergert, V. N. Antonov, W. A. Adeagbo, R. Matthias Geilhufe, H. Ben Hamed, *Phys. Status Solidi B* **2020**, *257*, 1900671. (in this issue)
[44] J. P. Perdew, in *Electronic Structure of Solids '91*, Physical Research, Vol. *17* (Eds: P. Ziesche, H. Eschrig), Akademie Verlag, Berlin **1991**, pp. 11–20.
[45] P. E. Blöchl, *Phys. Rev. B* **1994**, *50*, 17953.
[46] G. Kresse, D. Joubert, *Phys. Rev. B* **1999**, *59*, 1758.
[47] V. I. Anisimov, J. Zaanen, O. K. Andersen, *Phys. Rev. B* **1991**, *44*, 943.
[48] A. I. Liechtenstein, V. I. Anisimov, J. Zaanen, *Phys. Rev. B* **1995**, *52*, R5467.
[49] J. K. Shenton, D. R. Bowler, W. L. Cheah, *J. Phys.: Condens. Matter* **2017**, *29*, 445501.
[50] G. Rollmann, P. Entel, A. Rohrbach, J. Hafner, *Phase Transit.* **2005**, *78*, 251.

[51] S. W. Hoh, L. Thomas, G. Jones, D. J. Willock, *Res. Chem. Int.* **2015**, *41*, 9587.
[52] C. E. Rodrguez Torres, G. A. Pasquevich, P. M. Zélis, F. Golmar, S. P. Heluani, S. K. Nayak, W. A. Adeagbo, W. Hergert, M. Hoffmann, A. Ernst, P. Esquinazi, S. J. Stewart, *Phys. Rev. B* **2014**, *89*, 104411.
[53] Z. Li, R. Laskowski, T. Iitaka, T. Tohyama, *Phys. Rev. B* **2012**, *85*, 134419.
[54] B. Ribeiro, M. Godinho, C. Cardoso, R. P. Borges, T. P. Gasche, *J. Appl. Phys.* **2013**, *113*, 083906.
[55] S. L. Dudarev, G. A. Botton, S. Y. Savrasov, C. J. Humphreys, A. P. Sutton, *Phys. Rev. B* **1998**, *57*, 1505.
[56] F. D. Murnaghan, *Proc. Natl. Acad. Sci. USA* **1944**, *30*, 244.
[57] Code available at https://hutsepot.jku.at.
[58] P. Soven, *Phys. Rev.* **1967**, *156*, 809.
[59] B. L. Gyorffy, *Phys. Rev. B* **1972**, *5*, 2382.
[60] A. I. Liechtenstein, M. I. Katsnelson, V. P. Antropov, V. A. Gubanov, *J. Magn. Magn. Mater.* **1987**, *67*, 65.
[61] H. Ben Hamed, M. Hoffmann, W. A. Adeagbo, A. Ernst, W. Hergert, T. Hynninen, K. Kokko, P. Paturi, *Phys. Rev. B* **2019**, *99*, 144428.
[62] Z. M. Baiyee, C. Chen, F. Ciucci, *Phys. Chem. Chem. Phys.* **2015**, *17*, 23511.
[63] S. Förster, W. Widdra, *Surface Sci.* **2010**, *604*, 2163.
[64] R. A. Ribeiro, J. Andrs, E. Longo, S. R. Lazaro, *Appl. Surf. Sci.* **2018**, *452*, 463.
[65] R. Ribeiro, S. de Lazaro, L. Gracia, E. Longo, J. Andrs, *J. Magn. Magn. Mater.* **2018**, *453*, 262.
[66] D. von Dreifus, E. C. Pereira, A. J. A. de Oliveira, *Mater. Res. Express* **2015**, *2*, 116102.
[67] R. Wu, D. Wang, A. Freeman, *J. Magn. Magn. Mater.* **1994**, *132*, 103.
[68] O. Eriksson, G. Fernando, R. Albers, A. Boring, *Solid State Commun.* **1991**, *78*, 801.
[69] A. M. N. Niklasson, B. Johansson, H. L. Skriver, *Phys. Rev. B* **1999**, *59*, 6373.
[70] A. Freeman, H. Krakauer, S. Ohnishi, D. S. Wang, M. Weinert, E. Wimmer, *J. Magn. Magn. Mater.* **1983**, *38*, 269.